CrystEngComm

PAPER

Synthesis of hierarchical TiO$_2$ nanotube arrays assembled by anatase single crystal nanoparticles†

Tianci Zhang, Xiaoye Hu,* Ming Fang, Lide Zhang* and Zhaoming Wang

Hierarchical TiO$_2$ nanotube (HTNT) arrays assembled by anatase single crystal nanoparticles (NPs) were synthesized *via in situ* chemical etching of anodic TiO$_2$ nanotube (TNT) arrays. The process starts with the fabrication of smooth and crack-free anodic TNT arrays by employing an improved anodization method, which is used both as the starting material and a template for the synthesis of HTNT. The as-fabricated HTNT retains the tubular array structure as in the original anodic TNT, and the walls of HTNT possess a porous structure, consisting of anatase TiO$_2$ single crystal NPs. The formation mechanism of the HTNT was thoroughly investigated, proposing that a dissolution–recrystallization procedure of the anodic TNT under *in situ* chemical etching of hydrofluoric acid leads to the transformation from TNT arrays to HTNT arrays. Such HTNT structure has higher specific surface area and better crystallinity than the original anodic TNT, and possess one-dimensional passageways resulting in prominent advantages for the exchange and transportation of charge or mass, and could be an ideal candidate for many practical applications.

Introduction

Hierarchical structured micro and mesoporous materials assembled by specific morphology building components have attracted much attention in various fields, such as optoelectronics,[1] energy storage/conversion,[2] chemical sensors,[3] photocatalysis,[4] biochemistry,[5,6] *etc.* In many investigations the hierarchical structured materials have demonstrated improved performances, owing to the specific surface area resulting from the porous structures and specific morphology of building units. To date, various strategies have been developed to assemble highly organized architectures with building blocks based on different driving mechanisms, including CVD,[7] hydrothermal,[8] sacrificial template methods,[9,10] *etc.* Most of the works focused on the synthesis of spheres,[11] cages[12] or branched blocks.[7] Few reports referred to hierarchical porous nanotube arrays which might be more desirable for practical application. Herein, we employ a simple and reliable method to manipulate the primary building units and assemble them into ordered hierarchical nanotube arrays.

Titanium dioxide, as a well-known semiconductor material, has been extensively investigated in recent years. Among the three natural crystalline forms of TiO$_2$ (anatase, rutile and brookite), the anatase phase has superior optoelectronic and photochemical properties compared to rutile and brookite for applications in photocatalysis,[13–15] chemical sensors,[6,16] dye-sensitized solar cells,[17–19] water splitting,[20–22] *etc.* So far, anatase TiO$_2$ with various morphologies, including particles,[23,24] belts,[25] tubes,[4,26] wires,[18,27–29] spheres[9,11,30–32] *etc.*, have been synthesized and widely studied. Especially in the last few years, hollow hierarchical TiO$_2$ nanostructures, such as the anodic TiO$_2$ nanotube[33–35] and the alkali hydrothermal titanate nanotube,[36–39] have captured greater attention in view of their large specific surface area and their tubular structures. However, the anodic TiO$_2$ nanotubes are amorphous with poor properties, thus requiring calcination in air at about 500 °C for conversion into polycrystalline anatase. The alkali hydrothermal titanate nanotubes also need acid treatment for crystalization, but the products after treatment have poor crystallinity.[28] High crystallinity might be a beneficial factor for improving the properties of these materials. Generally speaking, single crystal is the optimal crystalline structure and has regular geometrical morphology with exposed active facets – single crystal anatase TiO$_2$ (octahedral structure),[40] for instance. Currently, the simple single crystal anatase TiO$_2$ nanostructures have been able to be fabricated by hydrothermal[40,41] or sol–gel methods,[42–44] but the synthesis of a specifically structured single crystal, like hollow hierarchical structures, is still difficult to achieve. Therefore, it is still a great challenge to develop a new approach to form hollow hierarchical TiO$_2$ nanostructures with anatase crystal nature.

Here we reported a simple hydrothermal approach to the synthesis of HTNT arrays assembled by single crystal anatase TiO$_2$ NPs, *via in situ* chemical etching of anodic TNT arrays in the presence of hydrogen fluoride. The as-fabricated HTNT

Key Laboratory of Materials Physics and Anhui Key Laboratory of Nanomaterials and Nanostructures, Institute of Solid State Physics, Chinese Academy of Sciences, Hefei, 230031, People's Republic of China. E-mail: hxy821982@issp.ac.cn (X. H.); ldzhang@issp.ac.cn (L. Z.); Fax: (+86) 551-559-1434; Tel: (+86) 551-559-1420

arrays retain the tubular structure as in the original anodic TNT arrays, and the walls of HTNT arrays possess a porous structure, consisting of anatase TiO_2 single crystal NPs. Such HTNT arrays have high specific surface area and good crystallinity, and possess one-dimensional interconnectivity properties, which would be more desirable for many practical applications, e.g., photodegradation of organic pollutants. Further detailed analysis of the structure and formation mechanism gave vital clues to understand the nanostructure growth mechanism, which would provide useful guidelines for future synthesis of special nanostructured materials.

Experimental

The synthesis of HTNT arrays involves two procedures: the fabrication of the high quality anodic TNT arrays with clean and smooth top surface, and the transformation of the HTNT arrays from the anodic TNT arrays.

The TNT arrays were fabricated by an improved two-step anodization of pure Ti foil in ethylene glycol containing hydrofluoric acid electrolyte at constant voltage. The first anodization step was carried out at 30 V for 3 h, producing the array of TNTs with small diameters; subsequently the applied voltage was increased to 100 V, and kept for 1 h to grow arrays of TNT with large diameters at the bottom of the slender TNT arrays. Finally, the as-fabricated samples with two-layer TNT arrays were treated by ultrasonic oscillation, removing the slender TNT arrays from samples, and leaving the array of TNTs with large diameters which remain a highly ordered TNT array with a clean top surface.

HTNT arrays were fabricated via in situ chemical etching of anodic TNT arrays by hydrothermal treatment in the presence of hydrofluoric acid. The TNT arrays with Ti substrate were put into sealed Teflon autoclaves containing 0.2–2 mL hydrofluoric acid with concentration of 4%.Then the autoclaves were placed into an oven and kept at 180 °C for 5 h. Finally the autoclaves were taken out of the oven and cooled down to room temperature. The obtained samples were washed with deionized water and dried at 100 °C in air to remove the residual F^- ions.

The morphologies of as-fabricated anodic TNT arrays and HTNT arrays were examined by field-emission scanning electron microscopy (FESEM; Sirion 200 FEG) and high resolution field-emission transmission electron microscopy (HRTEM; JEOL-2010, 200 kV). The crystal structure of HTNT arrays are investigated by selected area of electron diffraction (SAED) and determined by Raman spectroscopy with an Ar^+ laser excitation (514.5 nm) at room temperature. The specific surface area and pore size distributions of the as-fabricated TNT and HTNT samples were measured respectively by using a Micromeritics ASAP 2020 nitrogen adsorption/desorption apparatus at -195.85 °C. The adsorption isotherms were recorded as volume of gas adsorbed (cm^3 g^{-1} at STP) versus relative pressure near unity. The surface area of the samples was determined on the basis of the Brunauer–Emmett–Teller (BET) model and the pore size distribution was analyzed by using the Barrett–Joyner–Halenda (BJH) method.

The photocatalytic activities of the as-fabricated samples were examined by photodegrading a 20 mg L^{-1} methylene blue (MB) dye aqueous solution under the irradiation of 365 nm UV light (a

25 W low-pressure mercury UV lamp was used as the light source). Before the photodegradation experiment, all the samples were stirring in MB solution for 2 h in the dark to achieve the absorbance equilibrium of MB dye. The concentration of MB solution was monitored by the visible light absorbance at 664 nm using a Varian Cary-5E UV-vis spectrophotometer.

Results and discussion

Anodization of Ti foils in the electrolyte containing F^- ions could produce amorphous TNT arrays supported on the Ti substrate. However, the conventional anodization process would result in the bundling of disordered TNTs on the top surface due to the etching of the electrolyte to as-grown TNT arrays (see ESI, Fig. S1a†). Such disordered TNTs would have a negative effect on the practical applications of TNT arrays.[45] The previous approaches for the removal of the disordered TNTs mainly involve ultrasonic oscillations[46] and super-critical CO_2 cleaning.[45] The former may achieve the aim of removing the unordered TNTs; however, this results in meshes of micro-cracks in the TNT arrays or even the peeling off from the Ti substrate (see ESI, Fig. S1b and S1c†). The latter appears expensive and potentially dangerous, and not easy to control. In order to obtain highly ordered and crack-free TNT arrays with a smooth surface, here we used a two-step anodic method and an improved ultrasonic treatment towards this aim. The TNT arrays fabricated by a two-step anodic method (details can be found in experimental section) have a two-layered structure consisting of small-diameter TNTs on the top and the large-diameter TNTs on the bottom (see ESI, Fig. S2†). The joint of the two TNTs layer is mechanically weak because of the sudden change of tube diameter. When the two-layered TNT arrays are placed into the ultrasonic chamber, the power of the ultrasonic waves would be focused on the interface, resulting in the detachment of the two layers of the TNT arrays from one another and leaving the large-diameter TNT arrays on the bottom, supported on the Ti substrate (see ESI, Fig. S2b†). The remaining large-diameter ($\sim$170 nm) TNT arrays have a super-smooth top surface and no cracks on a large scale, as shown in Fig. 1 and ESI (Fig. S3–5).†

Subsequently, the as-fabricated TNT arrays with Ti substrate were put into the autoclave containing dilute hydrofluoric acid solution with concentration of 4% for hydrothermal treatment. During this process, TNTs would be etched in situ by
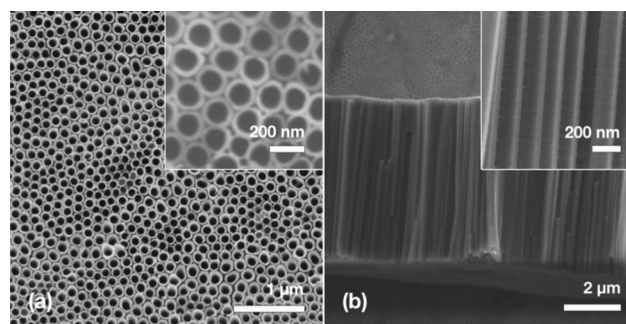

Fig. 1 SEM images of the anodic TNT arrays obtained by the improved two-step anodization method. The top view (a), and the cross-section (b). The partial enlarged views are shown in the insets, respectively.
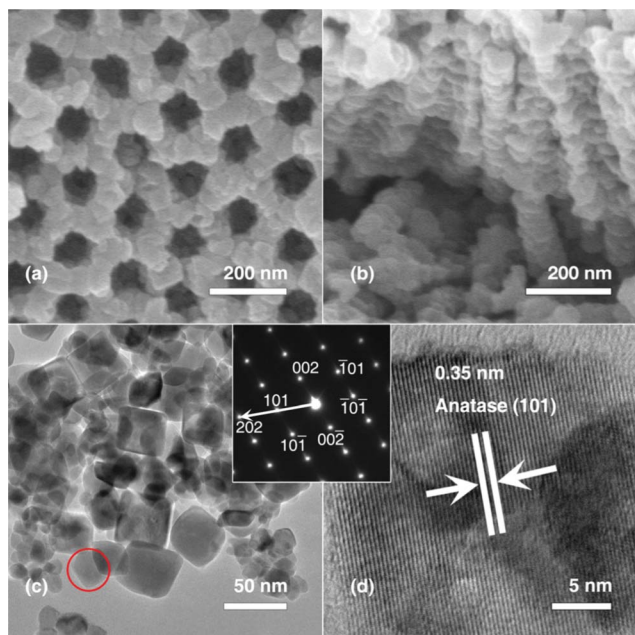
Fig. 2 SEM images of HTNT arrays in the top view (a), and the cross-section (b). (c) TEM image of dispersed TiO$_2$ NPs obtained after ultrasonic treatment of HTNT arrays. The inset is the related SAED image from HTNT (red circle in panel c). (d) Related HRTEM image of HTNT (red circle in panel c) and the lattice fringe.

hydrofluoric acid, forming HTNTs. Fig. 2a and 2b show the typical SEM images of HTNT arrays. The as-obtained HTNT arrays are open at the top end, and retain tubular array structures as in the original anodic TNTs. The walls of the tubes consist of many NPs, forming the porous structures (see Fig. 2a, 2b). With the help of sonication oscillation, dispersed NPs would be obtained from the collapse of HTNTs, which could be used as the TEM samples to deeply investigate their morphologies and structures. Fig. 2c displays the TEM image of the dispersed NPs, revealing that the NPs have relatively regular geometrical structures with an average size of around 50 nm. The inset of Fig. 2 is the SAED image from the region labeled by the red circle in Fig. 2c; the spot electron diffraction pattern indicates that the NP has a single-crystalline nature. The corresponding
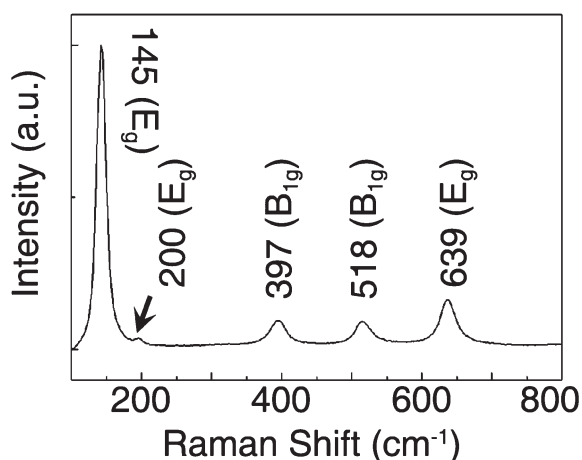
lattice fringes image also proves the high crystallinity of the NPs. Consistent with the SAED pattern, the distance between the adjacent lattice fringes are 0.35 nm, which can be assigned to the interplanar distance of anatase TiO$_2$ (101). As a further confirmation, the five sharp peaks at 145, 200, 397, 518 and 639 cm^{-1} in the Raman shift spectra of the sample (see Fig. 3) clearly indicate the anatase TiO$_2$ crystallographic phase Raman active modes with E$_g$, E$_g$, B$_{1g}$ and E$_g$ symmetry, respectively. All the above results prove that the HTNT arrays consist of anatase TiO$_2$ single crystal NPs, and inherit the tubular morphology of the TNT arrays after the hydrothermal treatment. Such hierarchically structural TNT arrays have both high specific surface area and the ideal crystallinity. Additionally, the ordered arrays might be also preferable in practical applications such as photocatalysis, water pollutant removal, dye-sensitized solar cells, *etc.*

As to the formation mechanism of the HTNT arrays, we proposed a feasible evolution process from amorphous TNT arrays to HTNT arrays *via in situ* chemical etching of hydrofluoric acid to the as-fabricated anodic TNT arrays. The evolution process could be ascribed to the dissolution–recrystallization procedure of amorphous TNT arrays, which is clearly described by the schematic diagram shown in Fig. 4. During the hydrothermal treatment process, the cavities inside TiO$_2$ tubes and the crevices among the neighboring TNTs were filled with the solution containing hydrogen fluoride due to the capillary effect. Under the condition of high temperature and pressure, the walls of TNT arrays would be gradually etched by hydrogen fluoride. The chemical reactions can be disclosed by the following equations:
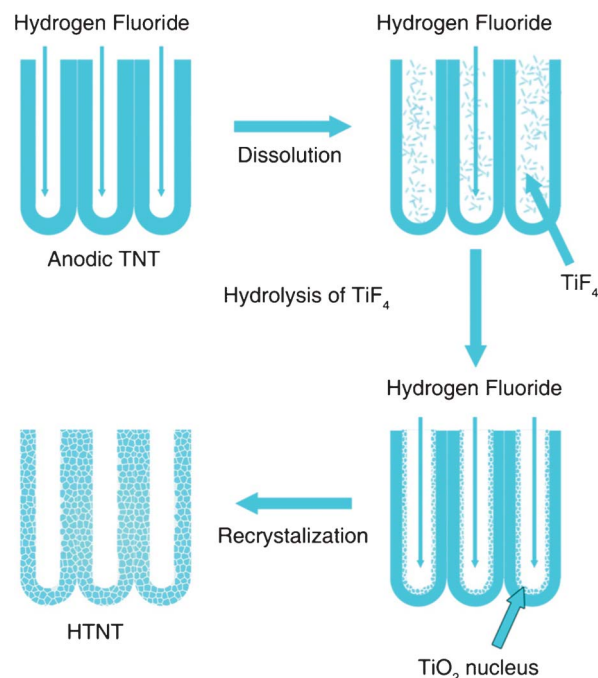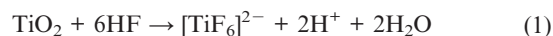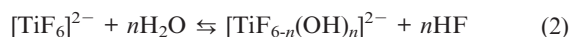
$$TiO_2 + 6HF \rightarrow [TiF_6]^{2-} + 2H^+ + 2H_2O \qquad (1)$$

Fig. 4 A schematic diagram of evolution process from anodic TNT arrays to HTNT arrays.

Fig. 3 The Raman spectrum of the as-prepared HTNT arrays sample.

$$[TiF_6]^{2-} + nH_2O \leftrightarrows [TiF_{6-n}(OH)_n]^{2-} + nHF \qquad (2)$$

$$[Ti(OH)_6]^{2-} + 2H^+ \rightarrow TiO_2 + 4H_2O \qquad (3)$$

Firstly, the internal and external wall surface of TNT arrays began to be dissolved by hydrogen fluoride (according to eqn (1)); forming $[TiF_6]^{2-}$ around the wall surfaces of TNT arrays (Fig. 4). As the dissolution process of the TNT wall continues, the concentration of hydrogen fluoride inside the nanotube lowered more quickly than that outside the nanotube, because the hydrogen fluoride inside the nanotube is difficult to rapidly exchange with that outside the nanotubes. When the concentration of hydrogen fluoride inside the nanotube lowers to a certain value, the $[TiF_6]^{2-}$ undergoes hydrolytic reaction to transform into TiO_2 NPs (according to eqn (2) and (3)), and dispersedly adsorbs on the surface of the non-dissociated TNT wall to grow (Fig. 4). Meanwhile, under the drive of gradient of hydrogen fluoride concentration between the inside of TNT arrays and solutions outside of TNT arrays, the hydrogen fluoride inside the TNT is regenerated by exchanging with the high concentration of hydrogen fluoride outside the TNT, resulting in the non-dissociated TNT walls to be further dissolved. It should be noted that the single crystal structure has higher acid endurance than the amorphous structure. Thus the hydrogen fluoride would first dissolve the remnant non-dissociated TNT wall, and then form more and more new TiO_2 nuclei near the initial TiO_2 nucleus. The accumulated TiO_2 nucleus gradually grew up and the small nucleus merged into large NPs under the non-equilibrium state of high temperature and pressure. Such dissolution–recrystallization are repeated, the HTNT would form when the TNT wall is completely dissolved (Fig. 4). Due to the chemical etching being accomplished *in situ*, the HTNT arrays inherits the organized tubular morphology of the anodic TNT arrays. Therefore, the anodic TNT arrays here served as not only the precursor but also the template for the formation of HTNT arrays.

During the formation of the HTNTs, the hydrogen fluoride played a key role for the formation of anatase TiO_2 NPs, and also mainly determines the morphologies of the HTNT. Fig. 5 shows the characteristics (including SEM images, TEM images and SAED spectrum) of typical samples fabricated by applying different concentration of hydrofluoric acid in hydrothermal treatments. When the volume of added hydrofluoric acid is 0.2 mL, the obtained HTNTs are built by hollow cubic-like NPs with an average size of 180 nm and exhibit an approximately square hollow profile (Fig. 5a–c). The SAED image of the cubic-like hollow TiO_2 shows that the NP is single crystal in nature corresponding to the anatase TiO_2 crystal phase, and the (100) crystal facet with relatively high surface energy is exposed (see inset of Fig. 5). When increasing the amount of hydrofluoric acid, the HTNT still keeps tubular array structures like the original anodic TNT arrays, but the size of TiO_2 NPs decreased. In the case of 1.0 mL hydrofluoric acid, the average size of TiO_2 NPs is down to about 50 nm (Fig. 2c). If the volume of hydrofluoric acid reaches 1.4 mL, the average size of TiO_2 is less than 30 nm (see Fig. 5d–f) and the TiO_2 NPs present a solid structure, and combine with each other closely to form the wall of the HTNT (Fig. 2a, 2b, and 5d–f). As shown in Fig. 5d–f, the HTNT arrays are composed by a large number of tiny TiO_2 NPs, which are closely gathered into a tubular structure, difficult to be scattered. Even though after a long ultrasonic oscillation treatment time, single NPs are hard to find in the TEM sample and the assembled hierarchical tube still exists (see Fig. 5f). For these agglomerated NPs, the SAED pattern (Fig. 5f) displays a polycrystalline ring-like pattern, which can be indexed to anatase (101), (004), (200) and (105) crystal faces. Further, the variation of the NPs size with the hydrogen fluoride concentration was investigated in detail by conducting a series of experiments with different volumes of hydrofluoric acid from 0.2 to 2 mL. The results show that the size of TiO_2 NPs decreases from average about 190 nm to less than 30 nm with the increase of the hydrogen fluoride from 0.2 to 2 mL, as shown in Fig. 6. In the case of less than or equal to 0.2 mL hydrofluoric acid, the NPs have a hollow cubic-like structure. Once the concentration of hydrofluoric acid exceeds 0.4 mL, the NPs begin to show a regular solid cubic-like morphology. If more than 1.4 mL hydrofluoric acid was applied, the morphology of NPs becomes irregular and generally remains with the sizes less than 30 nm.

To sum up these results, we suggest that the size of TiO_2 NPs can be tailored by manipulating the concentration of hydrofluoric acid added, thus achieving the control of the HTNT
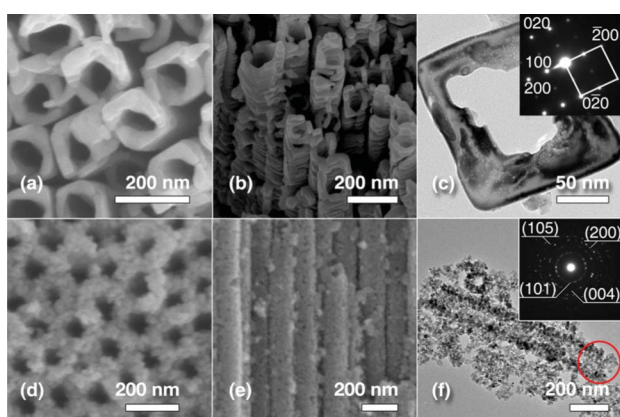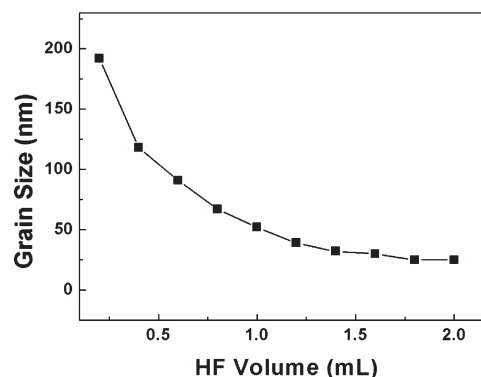

Fig. 5 SEM images in the top view (a), the side view (b); and the TEM image (c) of HTNT arrays fabricated by 0.2 mL hydrofluoric acid. The inset is electron diffraction pattern of single hollow cubic-like TiO_2 NP. SEM images in the top view (d), the side view (e); and the TEM image (f) of HTNT arrays fabricated by 1.4 mL hydrofluoric acid. The inset is the SAED image corresponding to the red circle area.

Fig. 6 Dependence of HTNT NPs size on volume of hydrofluoric acid in hydrothermal treatment.

Table 1 BET surface area of amorphous, annealed TNT arrays and HTNT arrays fabricated by 0.2, 1 and 1.4 mL hydrofluoric acid

	TNT arrays		HTNT arrays fabricated by different concentration of hydrofluoric acid		
Samples	Amorphous	Annealed	0.2 mL	1 mL	1.4 mL
BET surface area ($m^2 g^{-1}$)	18.4	35.4	31.6	42.9	46.8

morphology. Moreover, such manipulation of the TiO_2 NPs making up the HTNT can result in the tuning of the specific surface area of HTNT arrays. In order to monitor the variation of the specific surface area with TiO_2 NP size, the specific surface areas of three representative samples fabricated under 0.2, 1 and 1.4 mL hydrofluoric acid were measured respectively to compare with the initial amorphous TNT arrays and polycrystalline TNT arrays after annealing, as shown in Table 1 and Fig. S6 and S7.† It is obvious that the BET specific surface area of all the HTNT arrays is higher than the anodic TNT arrays due to the porous tubular structure assembled by the TiO_2 NPs and for the HTNT the BET specific surface area increases with the decreasing of the TiO_2 NPs size. The BET specific surface area of the annealed TNT is higher than the anodic TNT, and slightly higher than that of HTNT arrays fabricated by 0.2 mL hydrofluoric acid due to their relatively larger size and regular geometry shape of single crystal NPs in the 0.2 mL hydrofluoric acid HTNT arrays.

Generally, the high specific surface area has advantage to improve some properties of the materials in practical applications. Here we evaluated the photocatalytic activities of these HTNT and TNT arrays based upon the removal of methylene blue (MB) dye in aqueous solution as an example for confirming the improvement of properties originating from the high specific surface area and the unique structure. Fig. 7 displays the degradation curves of MB with the irradiation time, indicating that the photocatalytic activities of these samples are improved with the increase of the corresponding specific surface area. However, the photocatalytic activities are not absolutely determined by the specific surface area in our samples. For example, the specific surface area of HTNT arrays fabricated by 0.2 mL hydrofluoric acid is lower than the annealed TNT, but its photocatalytic activity is superior. We attributed this abnormal

phenomena to the better crystallinity and exposed active crystal facets of the single crystal TiO_2 NPs building the HTNT arrays, which have been confirmed in our previous work.[32]

Conclusions

In conclusion, HTNT arrays assembled by anatase single crystal NPs were synthesized *via in situ* chemical etching of anodic TiO_2 nanotube arrays. The walls of the as-fabricated HTNT are built by single crystal anatase TiO_2 NPs, forming a porous structure with high surface area. A dissolution–recrystallization evolution mechanism was proposed to interpret the formation mechanism of the HTNT arrays in detail, revealing that the HTNT arrays transform from the anodic TNT arrays *via in situ* chemical etching, inheriting the tubular structure of the anodic TNT. The concentration-dependent experiments confirmed that the shapes and sizes of the NPs comprising the HTNT arrays could be tailored by adjusting the hydrogen fluoride concentration in the hydrothermal treatment, meanwhile achieving manipulation of the specific surface area. The synthetic route could provide a rational strategy for other nanomaterial synthesis and structure design. Moreover, the unique structures of HTNT arrays are expected to be prominent candidates for applications in photocatalysis, energy conversion, water splitting and optoelectronics *etc.*

Acknowledgements

References

1 M. Devika, N. K. Reddy, A. Pevzner and F. Patolsky, *ChemPhysChem*, 2010, **11**, 809–814.
2 D. Deng, M. G. Kim, J. Y. Lee and J. Cho, *Energy Environ. Sci.*, 2009, **2**, 818–837.
3 L. Hao Feng, *Nanotechnology*, 2008, **19**, 405504.
4 J. M. Macak, M. Zlamal, J. Krysa and P. Schmuki, *Small*, 2007, **3**, 300–304.
5 P. Si, S. Ding, J. Yuan, X. W. Lou and D. H. Kim, *ACS Nano*, 2011, **5**, 7617–7626.
6 J. Li, X. Zhao, H. Wei, Z. Z. Gu and Z. Lu, *Anal. Chim. Acta*, 2008, **625**, 63–69.
7 K. A. Dick, K. Deppert, M. W. Larsson, T. Martensson, W. Seifert, L. R. Wallenberg and L. Samuelson, *Nat. Mater.*, 2004, **3**, 380–384.
8 C. Wu, L. Lei, X. Zhu, J. Yang and Y. Xie, *Small*, 2007, **3**, 1518–1522.
9 J. Yu, W. Liu and H. Yu, *Cryst. Growth Des.*, 2008, **8**, 930–934.
10 Y. Lei, S. Yang, M. Wu and G. Wilde, *Chem. Soc. Rev.*, 2011, **40**, 1247–1258.
11 J. H. Pan, G. Han, R. Zhou and X. S. Zhao, *Chem. Commun.*, 2011, **47**, 6942–6944.
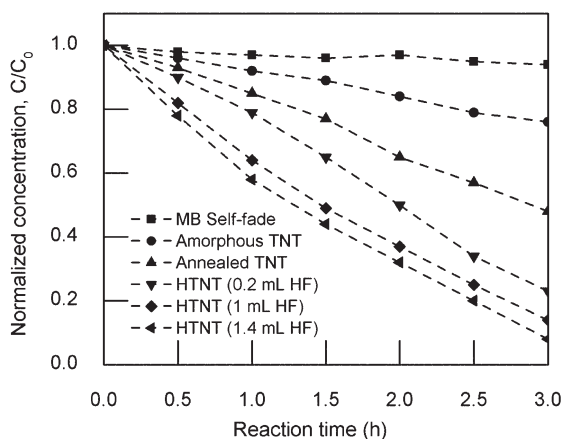12 S.-J. Liu, X.-X. Wu, B. Hu, J.-Y. Gong and S.-H. Yu, *Cryst. Growth Des.*, 2009, **9**, 1511–1518.

Fig. 7 Photocatalytic degradation of methylene blue dye solution by amorphous TNT arrays, TNT arrays after annealing at 500 °C for 5 h, HTNT arrays fabricated by 0.2, 1 and 1.4 mL hydrofluoric acid and the self-fade degradation of methylene blue dye under the UV light irradiation, respectively.

13 T. Yamamoto, N. Saso, Y. Umemura and Y. Einaga, *J. Am. Chem. Soc.*, 2009, **131**, 13196–13197.

14 A. Testino, I. R. Bellobono, V. Buscaglia, C. Canevali, M. D'Arienzo, S. Polizzi, R. Scotti and F. Morazzoni, *J. Am. Chem. Soc.*, 2007, **129**, 3564–3575.

15 H. Choi, A. C. Sofranko and D. D. Dionysiou, *Adv. Funct. Mater.*, 2006, **16**, 1067–1074.

16 S. J. Bao, C. M. Li, J. F. Zang, X. Q. Cui, Y. Qiao and J. Guo, *Adv. Funct. Mater.*, 2008, **18**, 591–599.

17 D. Chen, F. Huang, Y. B. Cheng and R. A. Caruso, *Adv. Mater.*, 2009, **21**, 2206–2210.

18 J. Jiu, S. Isoda, F. Wang and M. Adachi, *J. Phys. Chem. B*, 2006, **110**, 2087–2092.

19 M. Adachi, Y. Murata, J. Takao, J. Jiu, M. Sakamoto and F. Wang, *J. Am. Chem. Soc.*, 2004, **126**, 14943–14949.

20 J. Blomquist, L. E. Walle, P. Uvdal, A. Borg and A. Sandell, *J. Phys. Chem. C*, 2008, **112**, 16616–16621.

21 S. K. Mohapatra, K. S. Raja, V. K. Mahajan and M. Misra, *J. Phys. Chem. C*, 2008, **112**, 11007–11012.

22 J. Tang, J. R. Durrant and D. R. Klug, *J. Am. Chem. Soc.*, 2008, **130**, 13885–13891.

23 X. Y. Ma, Z. G. Chen, S. B. Hartono, H. B. Jiang, J. Zou, S. Z. Qiao and H. G. Yang, *Chem. Commun.*, 2010, **46**, 6608–6610.

24 Y. G. Seo, M. A. Kim, H. Lee and W. Lee, *Sol. Energy Mater. Sol. Cells*, 2011, **95**, 332–335.

25 R. Ma, K. Fukuda, T. Sasaki, M. Osada and Y. Bando, *J. Phys. Chem. B*, 2005, **109**, 6210–6214.

26 C. Richter, Z. Wu, E. Panaitescu, R. J. Willey and L. Menon, *Adv. Mater.*, 2007, **19**, 946–948.

27 E. Formo, E. Lee, D. Campbell and Y. Xia, *Nano Lett.*, 2008, **8**, 668–672.

28 Y. X. Yu and D. S. Xu, *Appl. Catal., B*, 2007, **73**, 166–171.

29 Y. Lei, L. D. Zhang, G. W. Meng, G. H. Li, X. Y. Zhang, C. H. Liang, W. Chen and S. X. Wang, *Appl. Phys. Lett.*, 2001, **78**, 1125–1127.

30 S. Ding, J. S. Chen, Z. Wang, Y. L. Cheah, S. Madhavi, X. Hu and X. W. Lou, *J. Mater. Chem.*, 2011, **21**, 1677–1680.

31 W. Ho, J. C. Yu and S. Lee, *Chem. Commun.*, 2006, 1115–1117.

32 X. Hu, T. Zhang, Z. Jin, S. Huang, M. Fang, Y. Wu and L. Zhang, *Cryst. Growth Des.*, 2009, **9**, 2324–2328.

33 O. K. Varghese, M. Paulose and C. A. Grimes, *Nat. Nanotechnol.*, 2009, **4**, 592–597.

34 J. M. Macak, H. Tsuchiya, L. Taveira, S. Aldabergerova and P. Schmuki, *Angew. Chem., Int. Ed.*, 2005, **44**, 7463–7465.

35 M. Paulose, K. Shankar, S. Yoriya, H. E. Prakasam, O. K. Varghese, G. K. Mor, T. A. Latempa, A. Fitzgerald and C. A. Grimes, *J. Phys. Chem. B*, 2006, **110**, 16179–16184.

36 X. Sun and Y. Li, *Chem.–Eur. J.*, 2003, **9**, 2229–2238.

37 A. Nakahira, T. Kubo and C. Numako, *Inorg. Chem.*, 2010, **49**, 5845–5852.

38 J. Huang, Y. Cao, M. Wang, C. Huang, Z. Deng, H. Tong and Z. Liu, *J. Phys. Chem. C*, 2010, **114**, 14748–14754.

39 D. V. Bavykin, A. N. Kulak and F. C. Walsh, *Langmuir*, 2011, **27**, 5644–5649.

40 H. G. Yang, C. H. Sun, S. Z. Qiao, J. Zou, G. Liu, S. C. Smith, H. M. Cheng and G. Q. Lu, *Nature*, 2008, **453**, 638–641.

41 F. Amano, O.-O. Prieto-Mahaney, Y. Terada, T. Yasumoto, T. Shibayama and B. Ohtani, *Chem. Mater.*, 2009, **21**, 2601–2603.

42 T. Sugimoto, X. Zhou and A. Muramatsu, *J. Colloid Interface Sci.*, 2003, **259**, 53–61.

43 K. Kanie and T. Sugimoto, *Chem. Commun.*, 2004, 1584–1585.

44 J. Lin, Y. Lin, P. Liu, M. J. Meziani, L. F. Allard and Y. P. Sun, *J. Am. Chem. Soc.*, 2002, **124**, 11514–11518.

45 K. Zhu, T. B. Vinzant, N. R. Neale and A. J. Frank, *Nano Lett.*, 2007, **7**, 3739–3746.

46 H. E. Prakasam, K. Shankar, M. Paulose, O. K. Varghese and C. A. Grimes, *J. Phys. Chem. C*, 2007, **111**, 7235–7241.